IEEE Access
Multidisciplinary | Rapid Review | Open Access Journal

Received December 30, 2021, accepted January 12, 2022, date of publication January 20, 2022, date of current version January 31, 2022.

Digital Object Identifier 10.1109/ACCESS.2022.3145023

Target Altitude Estimation in Over-the-Horizon Radar

YIMIN D. ZHANG[1], (Fellow, IEEE), AMMAR AHMED[2], (Member, IEEE), AND BRAHAM HIMED[3], (Fellow, IEEE)

[1]Department of Electrical and Computer Engineering, Temple University, Philadelphia, PA 19122, USA
[2]Advanced Safety and User Experience, Aptiv PLC, Agoura Hills, CA 91301, USA
[3]Distributed RF Sensing Branch, Air Force Research Laboratory, AFRL/RYMS, Dayton, OH 45433, USA

Corresponding author: Yimin D. Zhang (ydzhang@temple.edu)

The work of Yimin D. Zhang and Ammar Ahmed was supported in part by the Contract with Matrix Research, Inc., for research sponsored by the Air Force Research Laboratory under Contract FA8650-14-D-1722. The work of Yimin D. Zhang was also supported in part by the Contract with Altamira Technologies Corporation for research sponsored by the Air Force Research Laboratory under Contract FA8650-18-C-1055.

ABSTRACT Doppler signatures of local multipath signals provide useful information for target altitude estimation in over-the-horizon radar surveillance. In this paper, we develop a method to improve the resolution of these multipath Doppler signatures and enable enhanced altitude estimation of aircraft target which maintains a constant altitude. Moreover, we consider the impact of ionospheric layer motion on target parameter estimation and show that target parameters can be estimated under both stationary as well as time-varying ionospheric layer conditions. In order to improve the resolution and estimation accuracy of the target parameters and ionosphere velocity with a significantly reduced complexity, we exploit a frequency focused transform to the de-chirped target signals for dimension reduction before applying a least absolute shrinkage and selection operator (LASSO)-based high-resolution spectrum estimation technique. The proposed strategy outperforms fractional Fourier transform and classical subspace-based frequency estimation methods with a much lower computational complexity. The effectiveness of the proposed approach is especially evident for challenging cases where the multipath signal components have spectrally close Doppler signatures. Simulation results confirm the effectiveness of the proposed method.

INDEX TERMS Doppler signature, dynamic ionosphere, fractional Fourier transform, over-the-horizon radar, target geo-location, time-frequency analysis.

I. INTRODUCTION

Sky-wave over-the-horizon radar (OTHR) systems provide wide-area long-range surveillance far beyond the limit of the earth horizon [1]–[5]. Unlike other modern radar systems that use wideband signals and provide accurate localization of line-of-sight targets, OTHR systems are designed to monitor non-line-of-sight targets through the utilization of ionospheric reflections using narrowband signals whose bandwidth is determined based on the ionospheric conditions. These facts make accurate target geo-location, particularly the estimation of the target altitude, very challenging.

Target detection, localization and tracking are important objectives in OTHR operations [6]–[8]. The target altitude information is particularly valuable for target classification and perception. Direct estimation of target altitude is difficult due to several reasons, including the low-range resolution associated with the narrowband radar signal and the inaccuracy in the estimated ionosphere parameters. Therefore, great efforts have been dedicated to achieve this goal [9]–[15]. In [9], the authors obtained a matched-field estimate of aircraft altitude by exploiting multiple OTHR dwells and the altitude-dependent structure of the local multipath rays resulting from reflections local to the aircraft. This work was extended in [10] where the altitude and altitude rate were jointly estimated by investigating the effects of a constant altitude rate on the local multipath Doppler frequencies. Furthermore, a state-space model-based generalized altitude estimation technique was presented in [11], where the effect of random ionospheric and target motions was considered that degrades the dwell-to-dwell predictability of target returns. In [12], the instantaneous target altitude was estimated by

The associate editor coordinating the review of this manuscript and approving it for publication was Chengpeng Hao.

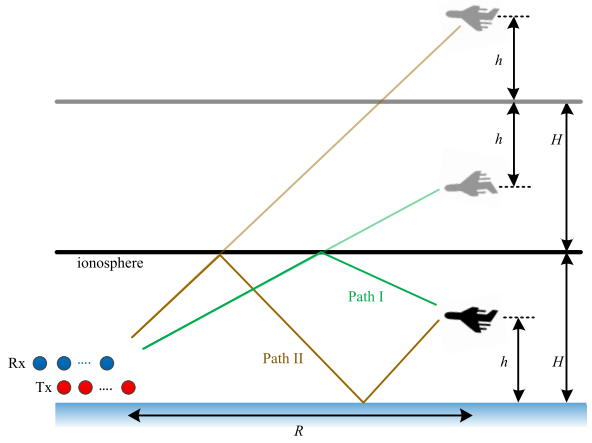

FIGURE 1. Flat-Earth model of local multipath propagation in an OTHR system.

employing time-frequency signal analysis of the time-varying local multipath Doppler signatures, and the initial state of the target parameters was obtained using the maximum *a posteriori* criterion. Target altitude estimation by exploiting two-dimensional multiple-input multiple-output (MIMO) radar using the multipath signal model and maximum likelihood estimation was discussed in [13]. An interesting study related to the experimental validation of target altitude estimation by exploiting local multipath propagation model was reported in [14].

According to the local multipath signal model [7], [12] illustrated in Fig. 1, signals through the direct path (directly reflected by an ionosphere layer) and the local multipath (that is further reflected by the specular ground/ocean surface) would generate slightly different Doppler signatures when a target maneuvers with a vertical velocity. Careful examination of this difference in Doppler signatures through high-resolution time-frequency analysis resolves the Doppler signatures of different local multipaths. The frequency difference between such Doppler signatures directly reveals the target vertical velocity, whereas the resolved Doppler signatures also enable enhanced target localization and tracking [12], [15]. Time-frequency analysis of such Doppler components is not trivial because the Doppler difference between the direct ionosphere path and the local multipath is very small [16]–[18]. The problem becomes even more challenging when the vertical motion of the target is accompanied by an azimuth rotation, which causes significant variations in the target Doppler frequencies [12], [15].

The scope of some past studies related to time-varying Doppler signature analysis was limited to the situations where the target experiences a maneuvering pattern that includes vertical motion [7], [12], [15]. In such work, the vertical target velocity was considered as the primary source that generates a detectable Doppler frequency difference between the multipath signals, which enables target altitude estimation. On the other hand, a target usually flies without changing its altitude during most of the flight time. In this case, the Doppler frequencies are difficult to resolve using existing methods, thus making difficult the estimation of the target altitude based on Doppler difference between the local multipath signals. As such, it is of a great interest to analyze the Doppler signatures, resolve them, and apply the proposed Doppler analysis for target altitude estimation. Moreover, the existing works [7], [12], [15] focus on the target parameter estimation during the stable ionosphere conditions. In practice, however, ionospheric conditions change over time [19] and it is important to estimate target parameters in such unstable ionosphere conditions.

The joint estimation of target range and ionosphere altitude was considered in [20] by exploiting the maximum likelihood estimation technique. However, the strategy exploited in [20] does not account for the time variation of the ionosphere and does not consider the target altitude. It is also noted that, the approach described in [20] relies on an accurate statistical model and, as a result, any deviation of the actual parameters from the assumed statistical model results in degraded parameter estimation performance.

In this paper, we revisit the problem in which the target maintains a constant horizontal speed without changing its altitude. Analysis results reveal that the Doppler signatures corresponding to different local multipath components still provide resolvable Doppler frequency differences. To gain more insights, we consider a flat-earth model and derive analytical formulations with approximations held under the assumption that the target range is much larger than the ionosphere height and the target altitude. We then verify the results using numerical simulations that are held without using the approximations. The approximated analysis show that the Doppler signatures of the target are well modeled as parallel chirp signals with Doppler frequency varying linearly with time. The frequency difference between the Doppler signatures is proportional to the carrier frequency, the ionosphere height, target altitude, and target horizontal velocity, but is inversely proportional to the square of the target range.

On the other hand, the height of the ionospheric layers, particularly the F-layer, is often time-varying. Such time-variation in the ionosphere altitude changes the Doppler signatures of the targets and induces additional frequency difference between the multipath Doppler signatures. We show that, depending on the related directions of the target motion and the ionosphere, their respective contributions to the Doppler frequency difference may be constructive or destructive, which respectively make the resolved Doppler signature easier or more difficult.

We verify our analysis with numerical simulations in different situations with and without variation in the ionosphere height. The time-varying Doppler signatures are analyzed for a coherent processing interval (CPI) and the results are presented using spectrograms. The fractional Fourier transform (FrFT) [21], [22] is used to detect the chirp rate as well as the frequency shift. These chirp parameters are used to estimate the target velocity and ionosphere velocity,

and accurate parameter estimation is achieved. Note that the use of FrFT permits us to exploit a long CPI. While time-frequency analysis with a long CPI is often used to enhance the target signal and to mitigate range migration of maneuvering targets [23], [24], our goal is to achieve an improved resolution of local multipath signal components with very small Doppler frequency differences.

We improve the frequency resolution of Doppler signatures by exploiting subspace-based methods, such as multiple signal classification (MUSIC) [25] and estimation of signal parameters via rotational invariant techniques (ESPRIT) [26], using the de-chirped data of the received signal. However, due to the long CPI, the resulting size of the data covariance matrix is large, making the eigenvalue decomposition required by these algorithms computationally expensive. For this reason, we propose a computationally efficient version of the least absolute shrinkage and selection operator (LASSO) [28] which employs a spectral focusing transform. This strategy enables LASSO to only focus on the area of our spectral interest and reduces the size of the received data without severely compromising the estimation performance. Furthermore, we show that the frequency resolution capability and the computational efficiency of the proposed approach is higher than that of MUSIC and ESPRIT, making it a more favorable strategy to resolve the Doppler signatures.

The contribution of this paper is summarized as follows:

- In the previous works that exploited three closely separated local multipath Doppler components, the vertical velocity of target is essential to offer sufficient intra-Doppler spectral separation between local multipath Doppler signatures, from which useful target velocity and altitude information can be derived. In this context, we reveal, for the first time, that a target maintaining a constant altitude also produces distinct local multipath Doppler signatures. While such Doppler difference is much smaller, it can still be resolved to enable extraction of important target information.
- We derive expressions for the average Doppler frequency of the local multipath Doppler signatures and their differences which are represented with respect to target velocity, target altitude, and ionosphere height. Depending on the directions of the target and ionosphere velocities, their contributions to the Doppler signatures add either constructively or destructively. Their constructive contributions result in a higher Doppler frequency difference, whereas their destructive contributions yield a closer separation, making their Doppler frequency separation difficult.
- The difference between the multi-component Doppler frequencies is small. To obtain accurate Doppler frequency estimation in such challenging situations with a low complexity, we develop a frequency focused LASSO algorithm which transforms the high-dimensional de-chirped target data to a low dimension while preserving the spectral content of interest. Compared to the classical subspace-based methods, the proposed approach provides improved frequency resolution and estimation accuracy with a low computational complexity.
- We develop a mechanism to accurately estimate the target altitude and velocity, along with the ionosphere velocity, based on the estimated parameters of the Doppler signatures associated with the target and clutter. The effectiveness of the proposed approach and its superiority over existing methods are verified using extensive simulation examples.

The remainder of the paper is organized as follows. Signal models and necessary preliminaries are introduced in Section II. In Section III, we present the mathematical relations for Doppler frequencies and target parameter estimation for the case of stable ionosphere. Section IV provides the analysis of the Doppler signatures induced by ionosphere as well as target motions and develops mathematical relations for target parameter estimation. In Section V, the Doppler frequency separation and estimation, which are required to estimate the target parameters, are considered by employing conventional fractional Fourier transform techniques. In Section VI, we propose a novel low-complexity frequency estimation method based on LASSO. Simulation results are presented in Section VII, whereas Section VIII concludes this paper.

Notations: We use lower-case (upper-case) bold characters to denote vectors (matrices). In particular, $(.)^{\mathrm{T}}$ and $(\cdot)^*$ respectively denote the transpose and conjugate operators of a matrix or vector. Moreover, $\|\cdot\|_1$ and $\|\cdot\|_2$ respectively denote the l_1- and l_2-norms of a vector, whereas diag$(\cdot)$ represents a diagonal matrix with the elements of a vector as the diagonal entries and $\mathbb{E}[\cdot]$ shows the expectation operator.

II. SIGNAL MODEL

A. MULTIPATH PROPAGATION GEOMETRY

Consider a flat-earth ionosphere model as shown in Fig. 1, where H is the height of the ionosphere layer, and h is the height of the target [12]. A coarse estimate of the initial height of the ionosphere layer, H, is considered known from ionosonde monitoring. In Fig. 1, the targets and propagation paths below the ionosphere are physically present, whereas those above the ionosphere are virtual images through the ionosphere layer and ground reflections for convenience of slant range computations.

As we observe in Fig. 1, the specular earth surface reflection near the target position yields different propagation paths of the emitted/received signals which are represented by the three groups of signal components. For the first component, both the emitted and received signals propagate along path I, whereas for the second component, both the emitted and received signals propagate along path II. The third component comprises two round-trip paths, one emitting along path I and returning along path II, and the other emitting along path II and returning along path I.

From Fig. 1, the one-way slant ranges l_1 of the direct path and l_2 of the local multipath can be expressed in terms of the ground range distance R, the ionosphere altitude H, and the target altitude h, as

$$l_1 = \left(R^2 + (2H - h)^2\right)^{\frac{1}{2}} = R\left(1 + \frac{4H^2 + h^2 - 4Hh}{R^2}\right)^{\frac{1}{2}}, \tag{1a}$$

$$l_2 = \left(R^2 + (2H + h)^2\right)^{\frac{1}{2}} = R\left(1 + \frac{4H^2 + h^2 + 4Hh}{R^2}\right)^{\frac{1}{2}}. \tag{1b}$$

Note that, in the above expressions, l_1, l_2, and R are time-varying, and H may or may not change over time. For notational simplicity, we omitted the explicit notation of (t) throughout this paper.

B. DOPPLER SIGNATURES

The slant range of the three round-trip paths (path 1: $[l_1, l_1]$, path 2: $[l_2, l_2]$, and path 3: $[l_1, l_2]$ or $[l_2, l_1]$) are given as:

$$L_1 = 2l_1, \quad L_2 = 2l_2, \quad L_3 = l_1 + l_2, \tag{2}$$

and the corresponding Doppler signatures are given by

$$f_{D,i} = -\frac{f_c}{c}\frac{dL_i}{dt}, \qquad i = 1, 2, 3, \tag{3}$$

where f_c denotes the carrier frequency and c is the velocity of the electromagnetic wave.

In practice, $R \gg H \gg h$ holds. To gain insightful observations of the relationship between the Doppler frequencies and the target motion as well as changes in the ionosphere height, we apply a first-order Taylor series expansion and approximation on Eq. (1) to get:

$$l_1 \approx R + \frac{4H^2 + h^2 - 4Hh}{2R} \approx R + \frac{2H^2 - 2Hh}{R}, \tag{4a}$$

$$l_2 \approx R + \frac{4H^2 + h^2 + 4Hh}{2R} \approx R + \frac{2H^2 + 2Hh}{R}. \tag{4b}$$

C. DOPPLER CHARACTERISTICS

For a maneuvering target, its horizontal and vertical motions collectively contribute to the target Doppler frequency characteristics. In previous works [7], [15], we mainly focused on the effect of the target motion, and both horizontal and vertical motions were considered. In this paper, we consider a different scenario where the target flies with a constant horizontal velocity and at a fixed altitude, whereas the height of the ionosphere is considered to vary with a constant speed. In this case, we obtain from Eq. (4b) that

$$\frac{\mathrm{d}l_1}{\mathrm{d}t} \approx \dot{R} + \frac{2H}{R^2}[2\dot{H}R - H\dot{R}] - \frac{2h}{R^2}[\dot{H}R - H\dot{R}], \tag{5a}$$

$$\frac{\mathrm{d}l_2}{\mathrm{d}t} \approx \dot{R} + \frac{2H}{R^2}[2\dot{H}R - H\dot{R}] + \frac{2h}{R^2}[\dot{H}R - H\dot{R}]. \tag{5b}$$

In this paper, we only consider the case where both $\dot{H}$ and $\dot{R}$ are constant. Note that, for both target and the ionosphere layer, the positive velocity is defined such that the value of the target range or the ionosphere height increases. The case with an unchanged ionosphere height is considered as a specific case with zero velocity, i.e., $\dot{H} = 0$.

The Doppler frequencies of the three different paths are then respectively given as

$$f_{D,1} = \bar{f}_D + \Delta f_D, \tag{6a}$$

$$f_{D,2} = \bar{f}_D - \Delta f_D, \tag{6b}$$

$$f_{D,3} = \bar{f}_D, \tag{6c}$$

where

$$\bar{f}_D = -\frac{f_c}{c}\frac{\mathrm{d}(l_1 + l_2)}{\mathrm{d}t} \approx -\frac{2f_c}{c}\dot{R} - \frac{4f_cH}{cR^2}[2\dot{H}R - H\dot{R}], \tag{7a}$$

$$\Delta f_D = -\frac{f_c}{c}\frac{\mathrm{d}(l_1 - l_2)}{\mathrm{d}t} \approx \frac{4f_ch}{cR^2}[\dot{H}R - H\dot{R}]. \tag{7b}$$

Therefore, the Doppler signatures for paths 1 and 2 are symmetric with respect to that of path 3. The average Doppler component, $\bar{f}_D$, is shared by all three paths, whereas the small frequency difference between the Doppler signatures corresponding to different paths is characterized by Δf_D. Note that both $\bar{f}_D$ and Δf_D are functions of $\dot{R}$ and $\dot{H}$. Moreover, the results in Eqs. (6) and (7) also apply to the Doppler signature of the clutter by letting $h = 0$ and $\dot{R} = 0$.

D. RECEIVED SIGNALS

The received signal at the OTHR receiver is the sum of three multipath Doppler components and can be expressed as follows:

$$x(t) = A_1 e^{\mathrm{j}\left(2\pi \int_0^T \bar{f}_D \mathrm{d}t + \phi_1\right)} + A_2 e^{\mathrm{j}\left(2\pi \int_0^T (\bar{f}_D + \Delta f_D)\mathrm{d}t + \phi_2\right)} + A_3 e^{\mathrm{j}\left(2\pi \int_0^T (\bar{f}_D - \Delta f_D)\mathrm{d}t + \phi_3\right)} + w(t), \tag{8}$$

where A_i denotes the respective signal magnitudes for the three chirp signals, and ϕ_i are their corresponding initial phases. The noise term $w(t)$ is considered to be circularly complex zero-mean white Gaussian noise of variance σ_w^2 and $\mathrm{j} = \sqrt{-1}$. The error analysis of such chirp signals in the time-frequency domain has been extensively discussed in [27].

As discussed in [12], [16], [17], a detectable value of Δf_D enables the individual estimation of $f_{D,1}, f_{D,2}$, and $f_{D,3}$. In this case, they can be used to estimate the parameters related to the target and the ionosphere layer. We considered three parameters, namely, the target altitude (h), the target speed ($\dot{R}$), and the ionosphere velocity ($\dot{H}$).

III. STABLE IONOSPHERE LAYER CASE

In this section, we analyze the Doppler signatures and target parameter estimation for the case where the altitude of the ionosphere layer does not change over time, i.e., $\dot{H} = 0$. The case with time-varying ionosphere height is considered in Section IV.

A. DOPPLER SIGNATURE ANALYSIS

When the ionosphere height does not change over time (i.e., $\dot{H} = 0$), the Doppler frequency generated by the ground clutter lies at zero frequency. For a target moving with a constant horizontal speed $\dot{R}$, the average and the difference Doppler frequencies of the target respectively become

$$\bar{f}_D \approx -\frac{2f_c}{c}\dot{R} + \frac{4f_c}{cR^2}H^2\dot{R}, \quad \Delta f_D \approx -\frac{4f_c}{cR^2}Hh\dot{R}. \tag{9}$$

Not surprisingly, the average target Doppler frequency is almost constant (with very small variations due to the changes in H and R). It is important to note that the difference Doppler frequency Δf_D is non-zero, and its magnitude is proportional to f_c, H, h, and $\dot{R}$, and inversely proportional to R^2. Since R does not significantly change during a CPI, the Doppler signatures can be well-characterized as three parallel chirps.

The required CPI depends on the Doppler difference between the local multipath signal components. For the parameters considered in this paper, the Doppler difference between the local multipath signal components is generally in the order of a fraction of a Hz. We know that the required observation time T to resolve two closely separated frequencies with a separation of Δf is given by $T \propto 1/\Delta f$. Therefore, a long CPI is typically required to resolve a small frequency separation between the three local multipath Doppler components generated by the target. Such a long CPI is supported by the current state-of-the-art [7], [17], [23], [24]. It is noted that the use of a long CPI may reduce the surveillance volume and frequency of revisits. However, a desirable frequency of revisits may be maintained by using multi-beam operation and time-frequency analysis for signals with missing samples [29]–[32]. The latter enables processing of discontinuous sensing data.

B. TARGET PARAMETER ESTIMATION

If the Doppler signatures are resolvable, the estimated values of $\bar{f}$ and Δf can be exploited to obtain the target parameters. From Eq. (9), we can estimate the target altitude as

$$\hat{h} = \frac{(R^2 - 2H^2)\Delta f_D}{2H\bar{f}_D}. \tag{10}$$

On the other hand, the target velocity is estimated from Eq. (9) as

$$\hat{\dot{R}} = -\frac{cR^2\bar{f}_D}{2f_c(R^2 - 2H^2)}. \tag{11}$$

IV. TIME-VARYING IONOSPHERE ALTITUDE CASE

In this section, we analyze the multipath Doppler signatures resulting from the target as well as the ionosphere for the case when the ionosphere height undergoes a change over time. For this purpose, the target and ionosphere velocity $\dot{H}$ is assumed to be constant over a CPI.

A. DOPPLER SIGNATURE ANALYSIS

The resulting Doppler signatures due to the target are expressed in Eq. (7). For this case, $\dot{H}$ contributes to both the average Doppler frequency and the difference Doppler frequency. Note that the difference Doppler frequency is now proportional to $\dot{H}R - H\dot{R}$. These parameters may add constructively or destructively, depending on the moving directions of the target and the ionosphere layer. As they are in the same order of magnitude, a destructive combination of their contributions will significantly reduce the difference Doppler frequency. For example, when the target moves towards the radar (with a negative velocity) and the ionosphere layer ascends (with a positive velocity), they add constructively, rendering a higher value of $|\Delta f_D|$ for easier separation of the three components. On the other hand, when one of these two components changes direction, $|\Delta f_D|$ becomes smaller and the Doppler signatures of the multipath signals become more difficult to resolve.

B. IONOSPHERE VELOCITY ESTIMATION FROM CLUTTER DOPPLER SIGNATURE

As we can see from the above discussion, one of the important parameters that affect the observed target Doppler signatures is the ionosphere velocity. While the OTHR system typically provides a coarse estimate of the ionosphere altitude from ionosonde outputs, it generally does not provide a timely update about the ionosphere velocity. As such, the ionosphere velocity should be estimated.

We consider the clutter Doppler frequencies in Eq. (7) by letting $\dot{R} = 0$ and $h = 0$. As such, the Doppler difference $\Delta f_{D,\text{clutter}} = 0$, as there are no local multipaths for the ground clutter, whereas the average Doppler frequency is given by

$$\bar{f}_{D,\text{clutter}} \approx -\frac{8f_cH}{cR}\dot{H}. \tag{12}$$

Hence, given a coarse knowledge of the initial target range and the initial ionosphere height, the ionosphere velocity can be estimated from the observed clutter Doppler frequency as

$$\hat{\dot{H}} = -\frac{cR\bar{f}_{D,\text{clutter}}}{8f_cH}. \tag{13}$$

In practice, the clutter Doppler signature may suffer from Doppler spreading and smearing due to the distributed nature of the clutter reflections. In the case of sea clutter, it is also contaminated by the ocean waves, which are typically characterized by the Bragg frequencies.

C. VARIATION RATE OF THE DOPPLER FREQUENCIES

From the approximated Doppler frequencies in Eq. (7), we can derive the chirp rate, i.e., the derivative of the average Doppler frequency $\bar{f}_D$ with respect to time, as:

$$\dot{\bar{f}}_D \approx -\frac{8f_c}{cR^3}(\dot{H}R - H\dot{R})^2, \tag{14}$$

which is apparently negative. The term $(\dot{H}R - H\dot{R})$ is the same as that in the Δf_D expression in Eq. (7). That is, when the motion of the target and the ionosphere constructively contribute to enlarge the Doppler difference, the Doppler signature has a more steep slope.

Note that this conclusion is derived for the case when the target and the ionosphere are moving with constant velocities. Specifically, for clutter, $\dot{R} = 0$, and the above expression becomes:

$$\dot{\bar{f}}_{D,\text{clutter}} \approx -\frac{8f_c}{cR}\dot{H}^2. \tag{15}$$

D. TARGET PARAMETER ESTIMATION

To estimate the target parameters and ionosphere velocity, we first isolate $\dot{R}$ from Eq. (8a), and obtain the following estimate of the target velocity:

$$\hat{\dot{R}} = -\frac{R^2}{R^2 - 2H^2}\left(\frac{c\bar{f}_D}{2f_c} + \frac{4H\dot{H}}{R}\right), \tag{16}$$

where the ionosphere velocity $\dot{H}$ is estimated from Eq. (13).

The target altitude h can be obtained by substituting the estimated $\dot{R}$ and $\dot{H}$ into Eq. (8b). Because the estimate of $\dot{R}$ depends on the average frequency $\bar{f}_D$, we express the estimate of the target altitude as

$$\hat{h} = \frac{cR\Delta f_D\left(R^2 - 2H^2\right)}{2cRH\bar{f}_D + 4f_c\dot{H}\left(R^2 + 2H^2\right)} \tag{17}$$

to explicitly show the dependence of $\hat{h}$ on both the average Doppler frequency, $\bar{f}_D$ and the difference Doppler frequency, Δf_D.

Note that, for target parameter estimation, a coarse estimate of the ionosphere height is assumed to be known from ionosonde monitoring. Since ionosonde monitoring does not necessarily provide real-time data of ionosphere, the ionosphere velocity can be estimated using Eq. (15). We can also utilize Eq. (15) to keep track of the ionosphere height between the ionosonde updates.

V. DOPPLER SIGNATURE SEPARATION

In this section, we discuss Doppler signature separation for OTHR by employing conventional time-frequency methods. A convenient way to visually analyze the time-varying frequency components is by constructing a spectrogram which is defined as the magnitude square of the short-time Fourier transform and is expressed for a signal $x(t)$ as

$$S(t,f) = \left|\int_{-\infty}^{\infty} x(u)g(t-u)\exp(-\mathrm{j}2\pi fu)\mathrm{d}u\right|^2, \tag{18}$$

where $g(t)$ is a window function.

Since all the received OTHR signals are regarded as parallel chirp signals, various methods, that have been developed for chirp parameter estimation, can be used to estimate the chirp parameters. In this paper, we use FrFT to estimate the chirp rate and frequency separation of the Doppler components. High-resolution frequency estimation will be discussed in the next section.

The α-angle FrFT of a signal $x(t)$, denoted as $\mathcal{X}_\alpha(u)$, is defined as [21], [22]:

$$\mathcal{X}_\alpha(u) = \int_{-\infty}^{\infty} x(t)\mathcal{K}_\alpha(t,u)\mathrm{d}t, \tag{19}$$

where

$$\mathcal{K}_\alpha(t,u) = \begin{cases} \sqrt{\dfrac{1-\mathrm{j}\cot(\phi)}{2\pi}}e^{\mathrm{j}\frac{u^2}{2}\cot(\phi)} \\ \quad \times e^{\mathrm{j}\frac{t^2}{2}\cot(\phi)}e^{-\mathrm{j}ut\csc(\phi)}, & \phi \neq k\pi, \\ \delta(t-u), & \phi = 2k\pi, \\ \delta(t+u), & \phi + \pi = 2k\pi, \end{cases} \tag{20}$$

k is a non-negative integer, u is the angular fractional frequency, and $\phi = \alpha\pi/2$. Once the optimal rotation angle α_{opt}, which aligns a chirp as a sinusoid in the fractional frequency domain, is determined, we can find the chirp rate using the following equation [21], [22]:

$$\hat{\mu} = -\cot\left(\alpha_{\text{opt}}\frac{\pi}{2}\right)\frac{f_s^2}{N}, \tag{21}$$

where $\hat{\mu}$ is the estimated chirp rate of the Doppler components and f_s is the pulse repetition frequency. Moreover, $N = f_sT$ is the number of samples used for calculating the FrFT and T is the coherent processing time.

The centroid frequency of the chirp can be found as [33]:

$$f_{\text{center}} = \frac{f_{\text{frft}}}{\sin(\alpha_{\text{opt}}\pi/2)}, \tag{22}$$

where $f_{\text{frft}} = u_{\text{peak}}f_s/\pi$ and u_{peak} is the estimated peak angular frequency of the individual chirp in the fractional domain.

VI. IMPROVED DOPPLER FREQUENCY ESTIMATION BASED ON FREQUENCY FOCUSED LASSO

The FrFT considered in the previous section is not a high frequency resolution technique. To analyze closely separated Doppler signatures, we propose a variant of the LASSO algorithm, which provides better frequency resolution and is computationally more efficient compared to existing methods.

Because all the Doppler components in $x(t)$ have the same chirp rate μ which can be estimated using Eq. (21), the estimated chirp rate $\hat{\mu}$ can be exploited to stationarize or de-chirp the received signal $x(t)$ as:

$$\begin{aligned} y(t) &= x(t)e^{-\mathrm{j}\pi\mu t^2} \approx x(t)e^{-\mathrm{j}\pi\hat{\mu}t^2} \\ &\approx A_1e^{\mathrm{j}(2\pi\bar{f}_Dt+\phi_1)} + A_2e^{\mathrm{j}(2\pi(\bar{f}_D+\Delta f_D)t+\phi_2)} \\ &\quad + A_3e^{\mathrm{j}(2\pi(\bar{f}_D-\Delta f_D)t+\phi_3)} + \tilde{w}(t), \end{aligned} \tag{23}$$

where $\tilde{w}(t)$ is the noise term. Because $y(t)$ contains multiple sinusoidal signal components, conventional high-resolution spectrum estimation methods, such as MUSIC [25] and ESPRIT [26], can be employed to resolve the three Doppler components from $y(t)$. However, due to the long CPI, these methods need to perform eigen- or singular-value decomposition of the data covariance matrix with a high dimension, which is computational very intensive. In the following, we propose a computationally efficient version of LASSO [28] by employing a spectral focusing transform to

focus only on the area of our spectral interest. This approach results in a more computationally efficient estimation of the Doppler signatures.

The proposed strategy exploits the spectral range of interest along with the estimated chirp rate estimated by the FrFT. Furthermore, it employs a LASSO-based regression on the reduced-dimension data to extract the sparse frequency estimates. For this purpose, we first adopt the signal model for a LASSO-based frequency estimation. The data vector of the sampled de-chirped signal $y(t)$ is constructed as:

$$\mathbf{y} = [y(1), y(2), \cdots, y(N)]^{\mathrm{T}}. \tag{24}$$

We construct an inverse Fourier transform dictionary matrix corresponding to a K-point fine grid of frequencies as:

$$\mathbf{A} = [\mathbf{a}(f_1), \mathbf{a}(f_2), \cdots, \mathbf{a}(f_K)], \tag{25}$$

where f_k denotes the kth frequency on the grid and

$$\mathbf{a}(f) = [1, e^{\mathrm{j}2\pi ft}, e^{\mathrm{j}4\pi ft}, \cdots, e^{\mathrm{j}2(N-1)\pi ft}]^{\mathrm{T}}. \tag{26}$$

It is important to note that, because we have the coarse knowledge of the spectral range of interest through the FrFT, the dictionary matrix $\mathbf{A}$ corresponds only to this spectral range so that the number of columns K is much lower than the case with the entire frequency band being taken into account. The LASSO algorithm performs the following optimization [28]:

$$\hat{\mathbf{r}} = \arg\min_{\mathbf{r}} \ \|\mathbf{A}\mathbf{r} - \mathbf{y}\|_2^2 + \eta \|\mathbf{r}\|_1, \tag{27}$$

where $\mathbf{r}$ is a $K \times 1$ sparse column vector whose non-zero elements select the columns in the dictionary matrix $\mathbf{A}$ corresponding to the estimated frequencies and η is the regularization parameter. The computational complexity of LASSO exploiting the least angle regression (LARS) algorithm [34] for $N \times 1$ data vector $\mathbf{y}$ and $K \times 1$ sparse vector $\mathbf{r}$ is $\mathcal{O}(K^3 + NK^2)$. In order to further reduce this computational load, we exploit again the coarse knowledge of the spectral range of interest to project $\mathbf{y}$ into the focused frequency band. For this purpose, we construct a $B \times N$ frequency focusing matrix $\mathbf{B}$ (with $B \ll K \ll N$) whose B rows collectively cover the focused spectral range of interest. The b-th row of $\mathbf{B}$ is given by

$$[\mathbf{B}]_b = \frac{1}{N}\left[e^{\mathrm{j}\left(\frac{N-1}{2}\right)b\frac{2\pi}{N}}, e^{\mathrm{j}\left(\frac{N-3}{2}\right)b\frac{2\pi}{N}}, \cdots, e^{-\mathrm{j}\left(\frac{N-1}{2}\right)b\frac{2\pi}{N}}\right], \tag{28}$$

which corresponds to a frequency sector centered at bf_s/N. The function of the matrix $\mathbf{B}$ is analogous to the beamspace processing matrix [35] used in beamspace direction-of-arrival estimation problems which enables data processing only for a specific spatial sector of interest and significantly reduces the computational complexity. The frequency focused data vector and the corresponding dictionary matrix take the following form:

$$\tilde{\mathbf{y}} = \mathbf{B}\mathbf{y}, \quad \tilde{\mathbf{A}} = \mathbf{B}\mathbf{A}. \tag{29}$$

TABLE 1. Simulation parameters.

Parameter	Notation	Value
Initial range	$R(0)$	2,500 km
Initial ionosphere height	$H(0)$	350 km
Aircraft altitude	$h(0)$	20 km
Target holizontal velocity	$\dot{R}$	300 m/s
Ionosphere vertical velocity	$\dot{H}$	55 m/s
Carrier frequency	f_c	16 MHz
Pulse repetition frequency	f_s	80 Hz
Number of slow-time samples	N	9,600

The new data vector $\tilde{\mathbf{y}}$ and the dictionary matrix $\tilde{\mathbf{A}}$ have sizes $B \times 1$ and $B \times K$, respectively. The resulting optimization for frequency estimation using the frequency focused LASSO approach takes the following form:

$$\begin{aligned}\hat{\mathbf{r}} &= \arg\min_{\mathbf{r}} \ \left\|\tilde{\mathbf{A}}\mathbf{r} - \tilde{\mathbf{y}}\right\|_2^2 + \eta \|\mathbf{r}\|_1 \\ &= \arg\min_{\mathbf{r}} \ \|\mathbf{B}(\mathbf{A}\mathbf{r} - \mathbf{y})\|_2^2 + \eta \|\mathbf{r}\|_1.\end{aligned} \tag{30}$$

The computational complexity of the frequency focused LASSO is reduced to $\mathcal{O}(K^3 + BK^2)$, which is much lower compared to the complexity of $\mathcal{O}(K^3 + NK^2)$ for LASSO and $\mathcal{O}(N^3/8)$ for the eigen-decomposition involved in MUSIC and ESPRIT.

VII. SIMULATION RESULTS

We consider a target flying at an altitude of 20 km at the initial range of 2,500 km. The ionosphere height is assumed to be 350 km. The OTHR is operating with a carrier frequency of 16 MHz and a pulse repetition frequency of 80 Hz. The input signal-to-noise ratio (SNR) for each Doppler component is assumed to be the same at -15 dB. The complete list of parameters is shown in Table 1 unless otherwise specified. A CPI of 120-second is considered as a default scenario, but an example of 60-second CPI is also presented. For computing spectrograms, a 4096-point Hamming window spanning a time period of 51.2 seconds is used. For chirp rate estimation using FrFT, we employ a two-stage strategy to find the rotation angle. In the first stage, we employ a 100-point grid between $\alpha = 0.995$ and $\alpha = 1.005$. In the second stage, we employ a 200-point grid centered around the peak of the first stage having a grid step size of $\Delta\alpha = 10^{-6}$.

First, we illustrate the simulation performance for classical time-frequency approaches of spectrogram and FrFT. In the subsequent sub-section, the performance of high-resolution frequency estimation algorithms and the proposed frequency focused LASSO will be discussed.

A. PERFORMANCE OF CONVENTIONAL FREQUENCY ESTIMATION METHODS

1) STABLE IONOSPHERE CASE

In this sub-section, we investigate Doppler frequency separation and target localization performance for a stable

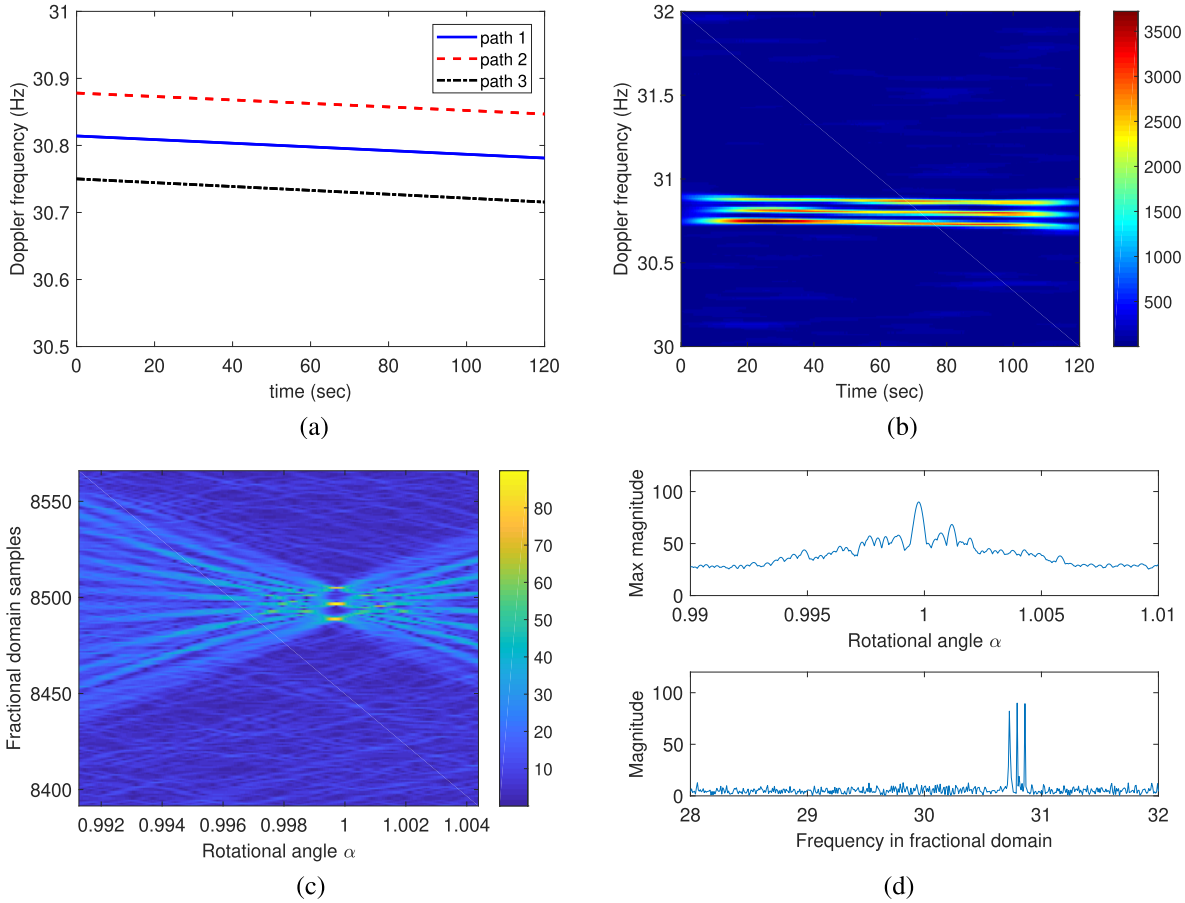

FIGURE 2. Doppler signatures of local multipath signals due to the motion of target for a stable ionosphere case ($\dot{H} = 0$). (a) Simulated Doppler signature; (b) Spectrogram; (c) Fractional Fourier transform; (d) Peak detection in rotation angle α and frequency domains. Figs. 2(b)–2(d) are computed with input SNR = −15 dB.

ionosphere ($\dot{H} = 0$). For the parameters listed in Table 1, the average target Doppler component $\bar{f}_D$ computed using Eq. (2) varies from 30.81 Hz to 30.78 Hz for an observation period of 120 seconds and is shown in Fig. 2(a). The value computed from the approximation in Eq. (9) varies from 30.74 Hz to 30.71 Hz. On the other hand, the Doppler difference Δf_D computed from the simulated slant range varies from 0.0640 Hz to 0.0657 Hz, and that computed from the approximated expression varies from 0.0717 Hz to 0.0738 Hz. Note that the difference due to the approximation is smaller in the average Doppler frequency and is higher in the Doppler difference. Note that the clutter has a zero Doppler frequency in this case due to a stationary ionosphere and is thus well separated from the target Doppler signature and can easily be filtered out.

Fig. 2(c) shows the FrFT results, with each column depicting the results corresponding to different rotation angle α. The three resolved peaks are detected when the correct rotation angle is chosen. To examine the values more clearly, we show the maximum magnitude with respect to the rotational angle in the upper panel of Fig. 2(d), and the peak is detected at $\alpha_{\text{opt}} = 0.999735$. In the lower panel of Fig. 2(d), we show the magnitude spectrum of the FrFT corresponding to the above-mentioned rotation angle, α_{opt}. The three peaks are clearly identified at 30.7260 Hz, 30.7926 Hz, and 30.8593 Hz in the fractional Fourier domain. As a result, the difference Doppler frequency is estimated to be 0.0666 Hz. According to Eq. (21), the obtained rotation angle can be mapped to the chirp rate of -2.77×10^{-4} Hz/s which is close to the actual chirp rate of -2.5×10^{-4} Hz/s.

Recall that the resolution capability of the local multipath components is a function of the value of Δf_D. Because signals are deemed resolvable when the CPI is inversely proportional to the difference Doppler frequency, the Doppler signatures considered in this case become resolvable with data observations as short as several seconds. Furthermore, as we discussed above, the Doppler difference is proportional to f_c, H, h, and $\dot{R}$, whereas it is inversely proportional to the square of the ground range. That is, higher values of f_c, H, h, and $\dot{R}$, or lower value of R will yield a larger value of Δf_D and render the detection of the three Doppler components easier.

From the estimated average Doppler frequency and the difference Doppler frequency, the target altitude is estimated as 18,555 meters, which is very close to the actual target altitude of 20, 000 meters.

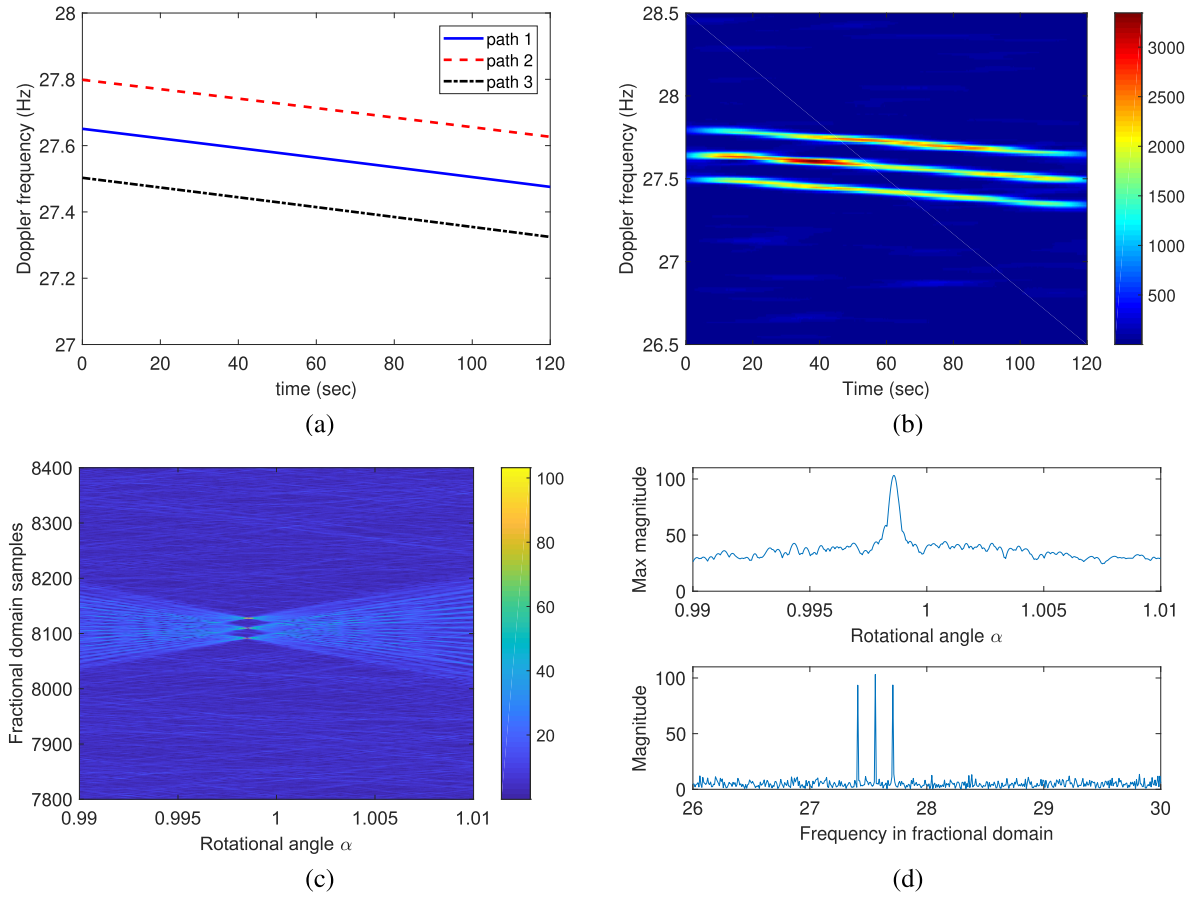

FIGURE 3. Doppler signatures of local multipath signals for the case of a moving ionosphere at $\dot{H} = 55$ m/s. (a) Simulated Doppler signature; (b) Spectrogram; (c) Fractional Fourier transform; (d) Peak detection in rotation angle α and frequency domains. Figs. 3(b)–3(d) are computed with input SNR = −15 dB.

2) DYNAMIC IONOSPHERE CASE

Note that the difference Doppler frequency is now proportional to $\dot{H}R - H\dot{R}$. For the parameters listed in Table 1, the magnitude of $\dot{H}R(0)$ is 1.375×10^8 m$^2/s$, whereas the magnitude of $H(0)\dot{R}$ is 1.05×10^8 m$^2/s$. The former is approximately 1.31 times the latter. They may add constructively or destructively, depending on the moving directions of the target and the ionosphere layer. As they are in the same order of magnitude, destructive combination of their contributions will significantly reduce the difference Doppler frequency.

To verify this, we perform simulations in two scenarios, where the ionosphere velocity respectively takes values of 55 m/s and −55 m/s [19]. The target velocity remains −300 m/s. The values of ionosphere velocity considered here represent the extreme cases of Doppler frequency estimates [19] and the lower values are much more typical. As such, the first case ($\dot{H} = 55$ m/s) renders a higher value of $|\Delta f_D|$, whereas the second case yields a smaller value of $|\Delta f_D|$.

Fig. 3 shows the first scenario, where the Doppler difference varies from 0.148 Hz to 0.151 Hz over the 120-second period. As expected, it is about 2.31 times the value obtained in the stable ionosphere case. In this case, the three components are clearly separated in the spectrogram and in the fractional Fourier domain. The rotation angle that yields the peak value in the upper panel of Fig. 3(d) is $\alpha_{\text{opt}} = 0.9986$, and the Doppler difference obtained from the lower panel of Fig. 3(d) is 0.150 Hz. The average Doppler frequency corresponding to the center position is 27.560 Hz, which matches well the middle-point value (at time of 60 seconds) of the simulated Doppler frequency, which varies from 27.651 Hz to 27.476 Hz. For this case, the chirp rate calculated using the rotation angle and Eq. (21) is -1.5×10^{-3} Hz/s, which again coincides well with the actual chirp rate of -1.46×10^{-3} Hz/s. It is noted that the Doppler frequencies in this case contain the contributions from the motions of both the target as well as the ionosphere layer.

Fig. 4 shows the second scenario, where the Doppler difference varies from −0.0198 Hz to −0.0204 Hz over the 120-second period. It confirms that the Doppler difference is about 31% the value obtained in the stable ionosphere case (notice the change of the sign as $\dot{H}R$ has a higher magnitude than $H\dot{R}$). In this case, the separation of the

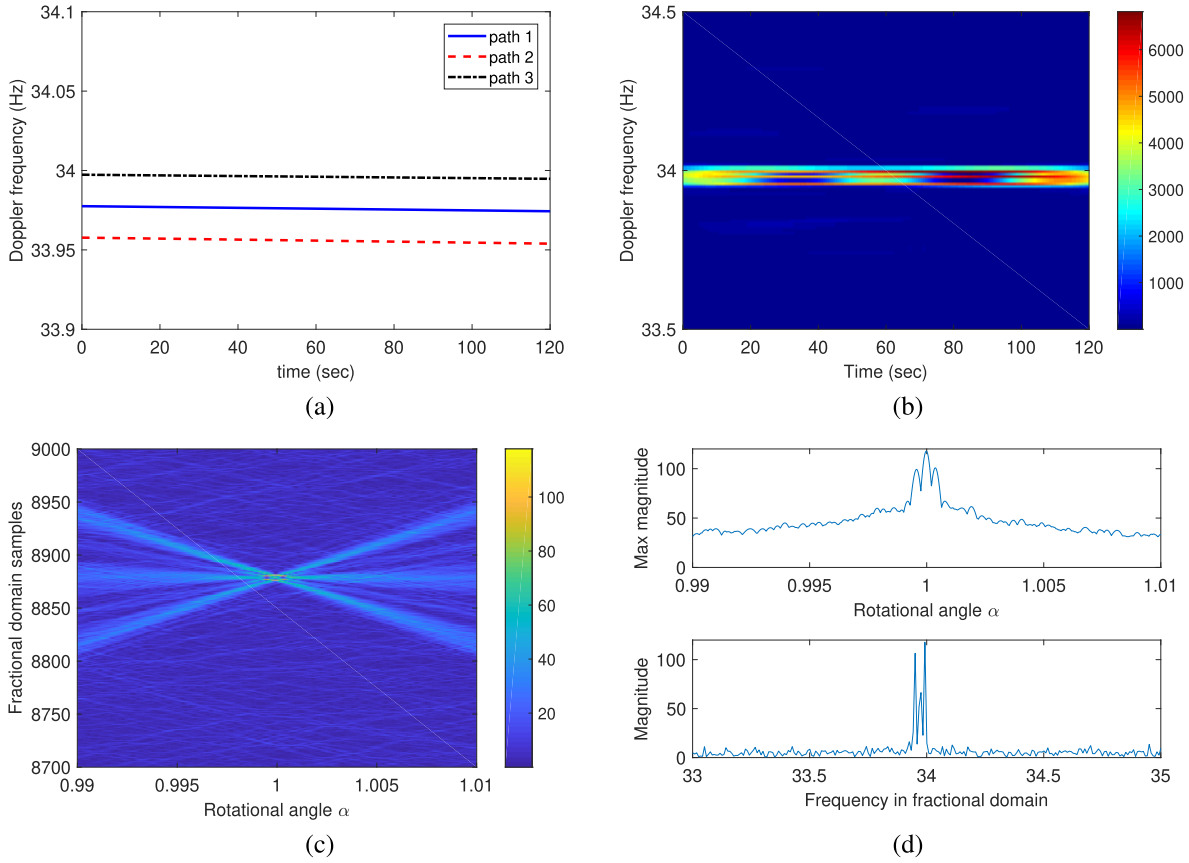

FIGURE 4. Doppler signatures of local multipath signals for the case of a moving ionosphere at $\dot{H} = -55$ m/s. (a) Simulated Doppler signature; (b) Spectrogram; (c) Fractional Fourier transform; (d) Peak detection in rotation angle α and frequency domains. Figs. 4(b)–4(d) are computed with input SNR = −15 dB.

TABLE 2. Summary of doppler frequency estimation results using conventional and proposed frequency estimation strategies.

Parameter	Actual	Fourier Transform	FrFT	Proposed
$\bar{f}_D$ ($\dot{H} = 0$ m/s)	30.814 Hz	30.80 Hz	30.792 Hz	30.812 Hz
$\bar{\Delta} f_D$ ($\dot{H} = 0$ m/s)	0.064 Hz	0.063 Hz	0.066 Hz	0.065 Hz
$\bar{f}_D$ ($\dot{H} = 55$ m/s)	27.651 Hz	failed	27.650 Hz	27.652 Hz
$\bar{\Delta} f_D$ ($\dot{H} = 55$ m/s)	0.148 Hz	failed	0.150 Hz	0.149 Hz
$\bar{f}_D$ ($\dot{H} = -55$ m/s)	33.978 Hz	33.979 Hz	33.979 Hz	33.978 Hz
$\bar{\Delta} f_D$ ($\dot{H} = -55$ m/s)	0.198 Hz	0.195 Hz	0.196 Hz	0.200 Hz

three components becomes less clear in both the spectrogram and in the fractional Fourier domain. In Fig. 4(b), we used a longer window size of 8, 192 points (which amounts to 102.4 seconds) for better frequency resolution. The rotation angle that yields the peak value in the upper panel of Fig. 4(d) is $\alpha_{\text{opt}} = 0.99997$, and the Doppler difference obtained from the lower panel of Fig. 4(d) is 0.0208 Hz (note that the time-frequency analysis cannot provide the sign information of the Doppler difference). The average Doppler frequency corresponding to the center position is 33.976 Hz, which still matches well the middle-point value of the simulated Doppler frequency, which varies from 33.978 Hz to 33.974 Hz. The chirp rate calculated using the fractional Fourier frequency for this case is -3.14×10^{-5} Hz/s, which is close to the actual chirp rate of -3.33×10^{-5} Hz/s.

Fig. 5 shows the actual clutter Doppler signatures corresponding to the two scenarios discussed above. For the former, the clutter Doppler frequency varies from −3.164 Hz to −3.219 Hz, whereas for the latter, it varies from 3.164 Hz to 3.108 Hz. This actual clutter frequency is obtained from Eqs. (1)–(3) by substituting $h = 0$. Note that Eq. (12), which is the basis for calculating the ionosphere velocity, provides the approximated clutter frequency.

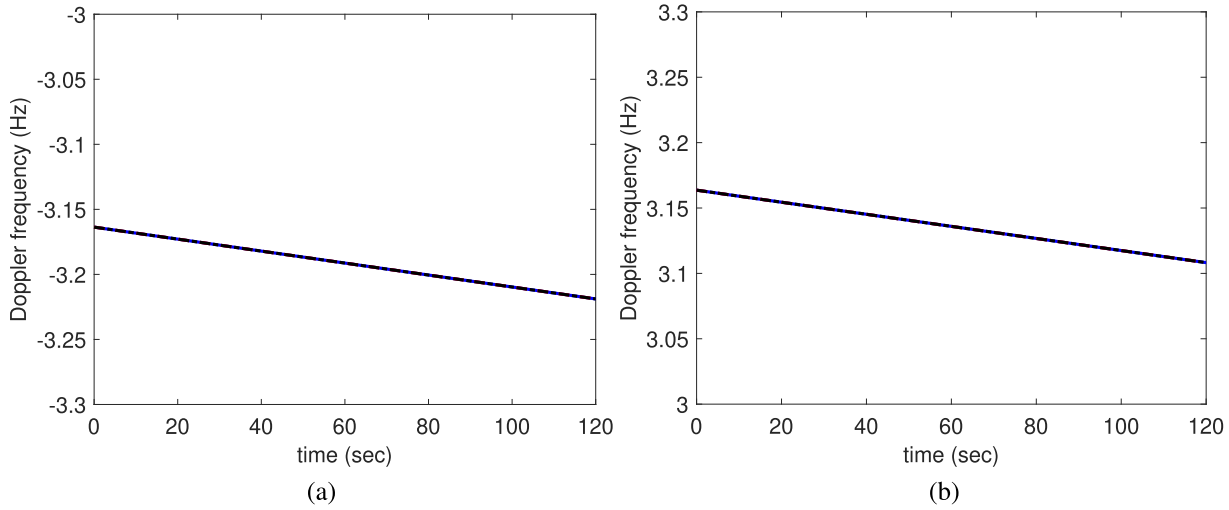

FIGURE 5. Doppler signatures of the clutter for a dynamic ionosphere case. (a) For an ionosphere velocity of 55 m/s; (b) For an ionosphere velocity of −55 m/s.

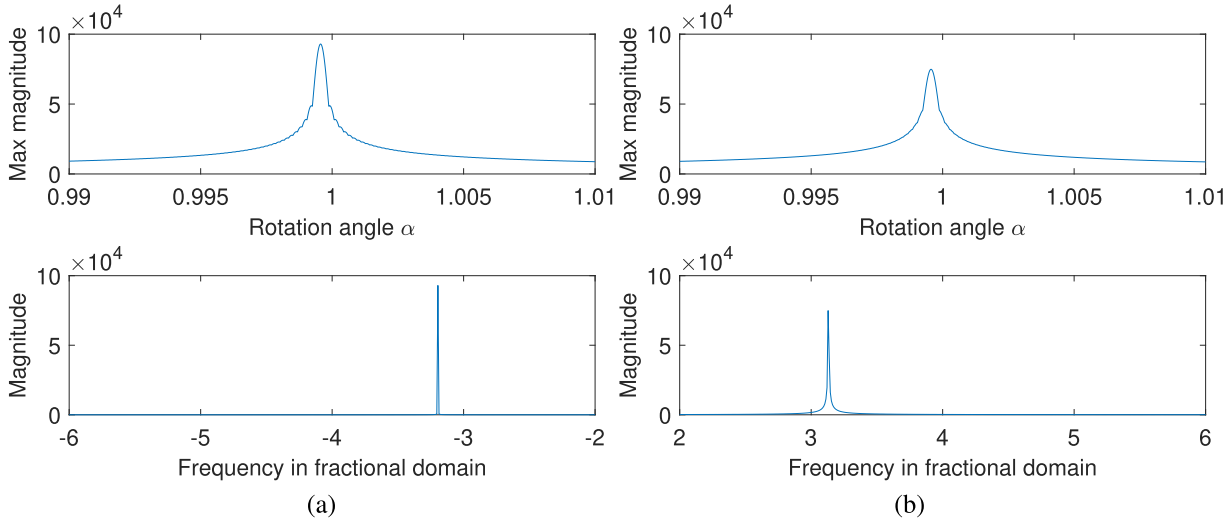

FIGURE 6. Fractional Fourier transform of the clutter for a dynamic ionosphere moving with velocity of (a) 55 m/s and (b) −55 m/s. The input CNR is 35 dB.

Recall that the difference Doppler component is proportional to $\dot{H}R - H\dot{R}$ which can add constructively or destructively depending on the values of $\dot{R}$ and $\dot{H}$. Therefore, extreme values of $\dot{H}$ are used in simulation results to emphasize the easiest and hardest cases of Doppler frequency resolution. It is evident from Fig. 3 that the resulting Doppler signatures have maximum spectral distance from each other, resulting in the easiest case for frequency resolution. On the other hand, Doppler signatures were extremely close to each other in Fig. 4, illustrating the most challenging case. As these extreme cases were successfully resolved, it is evident that all typical values for $\dot{H}$ will lead to resolvable Doppler signatures.

Fig. 6 shows the peak detection results of the FrFT for both cases of $\dot{H} = 55$ m/s and $\dot{H} = -55$ m/s. The input clutter-to-noise ratio (CNR) is 35 dB. The estimated rotation angle for both cases is $\alpha_{\text{opt}} = 0.99956$, which translates to a chirp rate of -4.607×10^{-4} Hz/s. The estimated Doppler frequency at the middle-point is -3.1955 Hz for the $\dot{H} = 55$ m/s case and 3.1288 Hz for the $\dot{H} = -55$ m/s case. To estimate the ionosphere velocity, we map the Doppler frequency at time 0 (seconds) so as to use the initial values of R and H. As such, the initial Doppler frequencies in both cases become -3.1672 Hz and 3.1571 Hz, and the corresponding estimates of the ionosphere velocity are 53.03 m/s and -52.85 m/s.

For the first case where the ionosphere moves with a velocity of 55 m/s, the estimated average Doppler frequency at the initial state is 27.47 Hz, and the difference Doppler frequency is 0.15 Hz. As a result, the estimated target velocity and target altitude are -298.95 m/s and 18, 526 m, respectively.

Similarly, for the second case where the ionosphere moves with a velocity of -55 m/s, the target velocity and altitude are estimated as -300.59 m/s and 22, 639 m, respectively. The

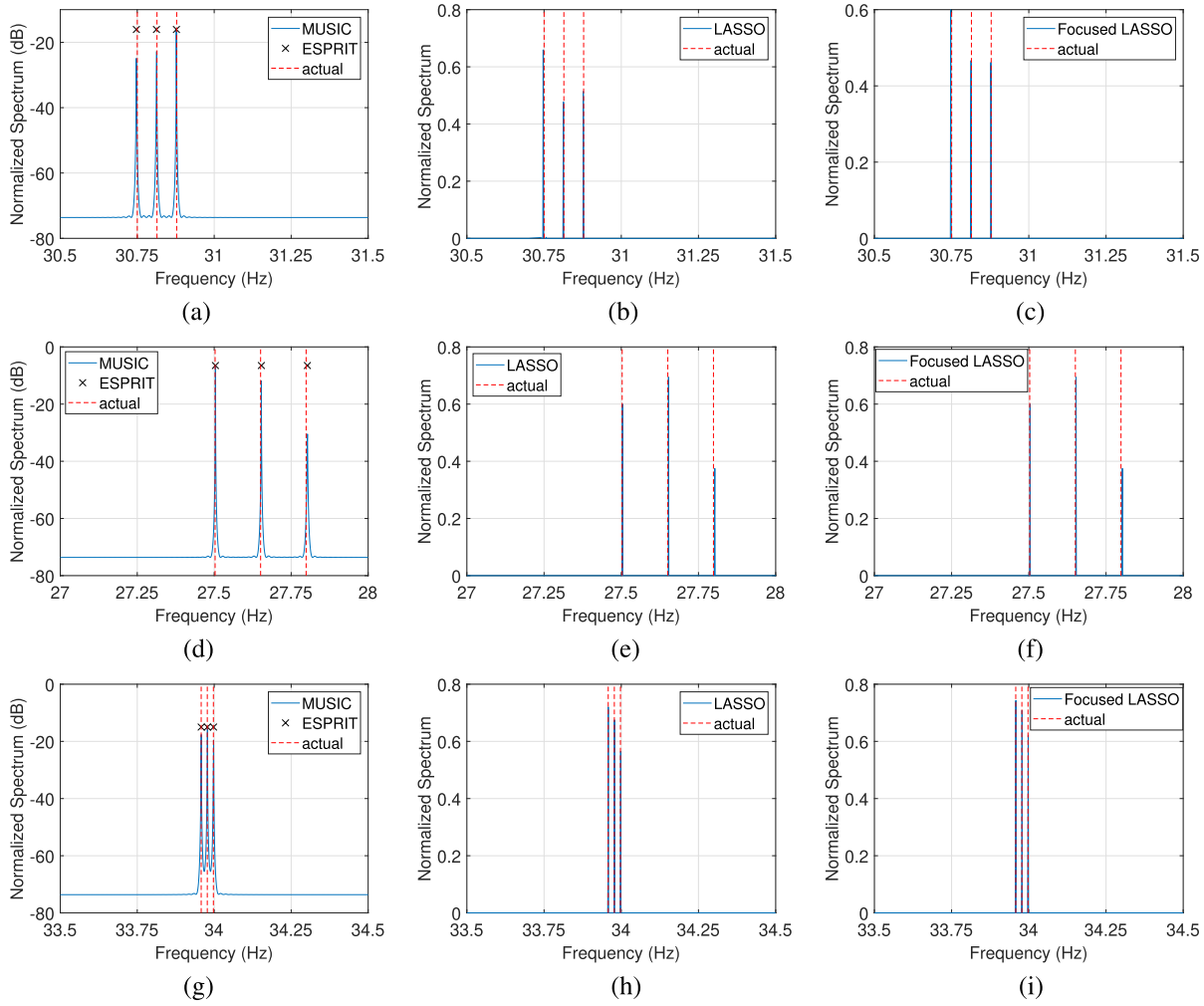

FIGURE 7. High resolution Doppler frequency estimation for the parameters in Table 1: (a)–(c) for a stable ionosphere case in Fig. 2, (d)–(f) for a moving ionosphere ($\dot{H} = 55$) case in Fig. 3, and (g)–(i) for a moving ionosphere ($\dot{H} = -55$ m/s) case in Fig. 4.

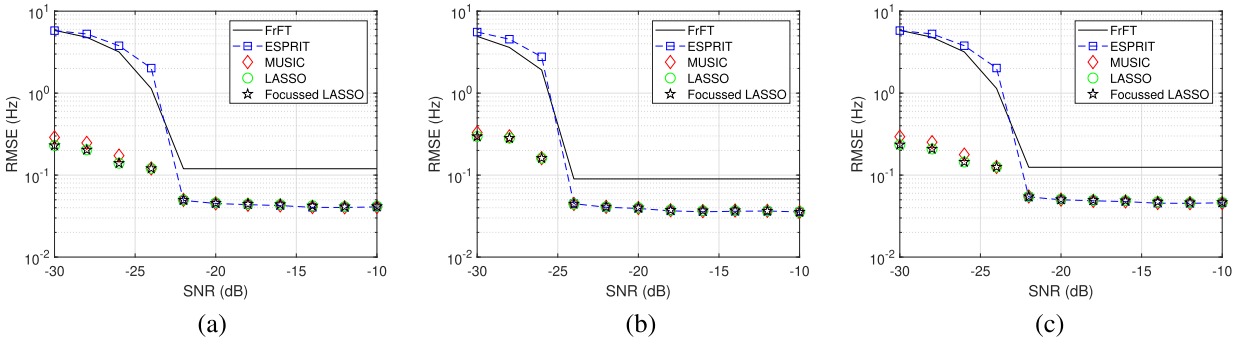

FIGURE 8. RMSE performance of the algorithms under consideration: (a) for a stable ionosphere case in Fig. 2, (b) for a moving ionosphere ($\dot{H} = 55$) case in Fig. 3, (c) for a moving ionosphere ($\dot{H} = -55$ m/s) case in Fig. 4.

estimated target velocity is accurate, whereas the estimated target altitude has some discrepancies due to the Taylor approximated model in computing the path lengths. It is important to note that existing methods for target parameter estimation do not consider the problem for ionosphere to experience any drift in the elevation velocity.

B. HIGH-RESOLUTION FREQUENCY ESTIMATION USING MUSIC, ESPRIT, LASSO, AND PROPOSED FOCUSSED LASSO

Now, we illustrate the performance of MUSIC, ESPRIT, and LASSO algorithms for Doppler frequency estimation and compare the results with the proposed frequency focused

LASSO algorithm. For MUSIC, LASSO, and frequency focused LASSO simulations, we use a ± 0.2 Hz spectral sector of interest around the frequency peak of FrFT and a frequency resolution of 0.002 Hz, rendering $K = 200$ frequency grid points for these methods. The results by ESPRIT are rounded-off for fair comparison. For frequency focused LASSO, we use $B = 60$ rows for the 1-Hz spectral sector. Note that all these algorithms are employed on the de-chirped version of the received signals. The estimated chirp rate in Eq. (21) is used to de-chirp the received OTHR signals. Note also the fact that $B \ll K \ll N$ results in a highly computationally efficient frequency estimation using the frequency focused LASSO.

For the scenarios depicted in Figs. 2–4, we employ high resolution frequency estimation algorithms discussed in this section. All the strategies presented in this section provide the same estimation performance for the three scenarios being considered, but the frequency focused LASSO requires a much lower computational complexity. For the cases of a stable ionosphere ($\dot{H} = 0$), positive ionosphere velocity ($\dot{H} = 55$ m/s), and negative ionosphere velocity ($\dot{H} = -55$ m/s), the corresponding target altitudes estimated using Eqs. (10) and (17) are 18,097 m, 18,545 m, and 21,768 m, respectively. The errors in the altitude estimates are primarily due to the Taylor approximation exploited in the data model.

For the three different simulation scenarios discussed here, we compare the numeric results of the proposed frequency focused LASSO strategy with FrFT and conventional Fourier transform in Table 2. Note that the conventional Fourier transform does not successfully resolve three Doppler signatures for all the scenarios due to the chirp nature of the frequency components. We can visually inspect from Figs. 2(a), 3(a), and 4(a) that the resulting Doppler components have the highest chirp rate for the case of $\dot{H} = 55$ m/s. Although the corresponding Doppler components for this case are well separated in the spectral domain with the highest value of Δf, the conventional Fourier transform fails to resolve the three Doppler signatures due to their high chirp rates. On the other hand, the proposed frequency focused LASSO approach provides better estimates of the three Doppler frequencies.

In order to compare all the algorithms considered in this paper, the root mean squared error (RMSE) of the three cases under consideration is plotted in Fig. 8 using 100 Monte Carlo trials. All the RMSE results show that the proposed frequency focused LASSO approach provides the same estimation performance as the LASSO but with a substantial reduction in the computational complexity, and is the most computationally efficient Doppler frequency estimation approach among all those being considered here. On average, the computation time of the MUSIC, ESPRIT, and LASSO for one trial is more than 2 minutes each, whereas the frequency focused LASSO provides frequency estimates in less than 2 seconds. The RMSE of the MUSIC, LASSO, and frequency focused LASSO is lower than the ESPRIT and FrFT for the -30 dB to -25 dB input SNR cases because of the narrow search range of ± 0.2 Hz around the FrFT peak. In summary, all the high-resolution algorithms provide comparable performance, but the frequency focused LASSO is most computationally efficient. The saturation region for SNR to be greater than -25 dB is due to the off-grid rounding effects of frequency grids. For fair comparison, the floating point accuracy of ESPRIT estimates is also kept the same as other algorithms by rounding-off the frequency estimates to the nearest grid point.

VIII. CONCLUSION

In this paper, we analyzed the Doppler signatures of a target with a constant horizontal velocity in an OTHR system. It is revealed that these Doppler signatures due to local multipath propagation can be characterized by parallel chirp signals and their frequency difference renders these signatures resolvable through time-frequency analyses. As such, the Doppler parameters of these signals, such as the average Doppler frequency and chirp rate, can be estimated. These parameters, in turn, enable the estimation of target altitude, target velocity, and ionosphere velocity. We investigated the performance of the proposed strategy by employing subspace-based frequency estimation methods, such as MUSIC and ESPRIT. Moreover, we proposed a reduced complexity version of LASSO by employing a frequency focusing transform. We argued that the existing classical frequency estimation methods exhibit high computational complexity and fail to resolve the target Doppler signatures in challenging cases. On the other hand, the proposed strategy provides high-resolution frequency estimates and is computationally efficient. Simulation results evidently demonstrate the feasibility of the proposed strategies for target altitude estimation.

REFERENCES

[1] J. M. Headrick and M. I. Skolnik, "Over-the-horizon radar in the HF band," *Proc. IEEE*, vol. 62, no. 6, pp. 664–673, Jun. 1974.
[2] L. F. McNamara, *The Ionosphere: Communications, Surveillance, and Direction Finding*. São Paulo, CA, USA: Krieger, 1999.
[3] Y. I. Abramovich, G. J. Frazer, and B. A. Johnson, "Principles of mode-selective MIMO OTHR," *IEEE Trans. Aerosp. Electron. Syst.*, vol. 49, no. 3, pp. 1839–1868, Jul. 2013.
[4] J. M. Headrick and S. J. Anderson, "HF over-the-horizon radar," in *Radar Handbook*, M. Skolnik, Ed. New York, NY, USA: McGraw-Hill, 2008.
[5] G. A. Fabrizio, *High Frequency Over-the-Horizon Radar: Fundamental Principles, Signal Processing, and Practical Applications*. New York, NY, USA: McGraw-Hill, 2013.
[6] K. L. Bell, "MAP-PF multi-mode tracking for over-the-horizon radar," in *Proc. IEEE Radar Conf.*, Atlanta, GA, USA, May 2012, pp. 326–331.
[7] Y. Zhang, M. G. Amin, and G. J. Frazer, "High-resolution time-frequency distributions for manoeuvring target detection in over-the-horizon radars," *IEE Proc. Radar Sonar Navig.*, vol. 150, no. 4, pp. 299–304, Aug. 2003.
[8] K. Lu and X. Liu, "Enhanced visibility of maneuvering targets for high-frequency over-the-horizon radar," *IEEE Trans. Antennas Propag.*, vol. 53, no. 1, pp. 404–411, Jan. 2005.
[9] M. Papazoglou and J. L. Krolik, "Matched-field estimation of aircraft altitude from multiple over-the-horizon radar revisits," *IEEE Trans. Signal Process.*, vol. 47, no. 4, pp. 966–976, Apr. 1999.
[10] M. Papazoglou and J. L. Krolik, "Estimation of aircraft altitude and altitude rate with over-the-horizon radar," in *Proc. IEEE Int. Conf. Acoust. Speech Signal Process.*, Phoenix, AZ, USA, Mar. 1999, pp. 2103–2106.

[11] R. H. Anderson, S. Kraut, and J. L. Krolik, "Robust altitude estimation for over-the-horizon radar using a state-space multipath fading model," *IEEE Trans. Aerosp. Electron. Syst.*, vol. 39, no. 1, pp. 192–201, Jan. 2003.
[12] Y. D. Zhang, J. J. Zhang, M. G. Amin, and B. Himed, "Instantaneous altitude estimation of maneuvering targets in over-the-horizon radar exploiting multipath Doppler signatures," *EURASIP J. Adv. Signal Process.*, vol. 2013, no. vol. 2013, p. 100, pp. 1–13, May 2013.
[13] Z. Luo, Z. He, X. Chen, and K. Lu, "Target location and height estimation via multipath signal and 2D array for sky-wave over-the-horizon radar," *IEEE Trans. Aerosp. Electron. Syst.*, vol. 52, no. 2, pp. 617–631, Apr. 2016.
[14] J. Praschifka, L. J. Durbridge, and J. Lane, "Investigation of target altitude estimation in skywave OTH radar using a high-resolution ionospheric sounder," in *Proc. Int. Radar Conf.*, Bordeaux, France, Oct. 2009, pp. 1–6.
[15] Y. D. Zhang, M. G. Amin, and B. Himed, "Altitude estimation of maneuvering targets in MIMO over-the-horizon radar," in *Proc. IEEE 7th Sensor Array Multichannel Signal Process. Workshop (SAM)*, Hoboken, NJ, USA, Jun. 2012, pp. 257–260.
[16] C. Ioana, M. G. Amin, Y. D. Zhang, and F. Ahmad, "Characterization of Doppler effects in the context of over-the-horizon radar," in *Proc. IEEE Radar Conf.*, Washington, DC, USA, 2010, pp. 506–510.
[17] C. Ioana, Y. D. Zhang, M. G. Amin, F. Ahmad, G. Frazer, and B. Himed, "Time-frequency characterization of micro-multipath signals in over-the-horizon radar," in *Proc. IEEE Radar Conf.*, Atlanta, GA, USA, May 2012, pp. 671–675.
[18] Y. D. Zhang and B. Himed, "Multipath Doppler difference estimation in over-the-horizon radar," in *Proc. IEEE Radar Conf.*, Oklahoma City, OK, USA, Apr. 2018, pp. 693–697.
[19] F. Bertoni, I. S. Batista, M. A. Abdu, B. W. Reinisch, and E. A. Kherani, "A comparison of ionospheric vertical drift velocities measured by digisonde and incoherent scatter radar at the magnetic equator," *J. Atmos. Solar-Terrestrial Phys.*, vol. 68, no. 6, pp. 669–678, Mar. 2006.
[20] J. Hu, M. Li, Q. He, Z. He, and R. S. Blum, "Joint estimation of MIMO-OTH radar measurements and ionospheric parameters," *IEEE Trans. Aerosp. Electron. Syst.*, vol. 53, no. 6, pp. 2789–2805, Dec. 2017.
[21] H. M. Ozaktas, M. A. Kutay, and Z. Zalevsky, *The Fractional Fourier Transform: With Applications in Optics and Signal Processing*. Hoboken, NJ, USA: Wiley, 2001.
[22] E. Sejdić, I. Djurović, and L. Stanković, "Fractional Fourier transform as a signal processing tool: An overview of recent developments," *Signal Process.*, vol. 91, no. 6, pp. 1351–1369, Jun. 2011.
[23] J. Xu, J. Yu, Y.-N. Peng, and X.-G. Xia, "Radon-Fourier transform for radar target detection, I: Generalized Doppler filter bank," *IEEE Trans. Aerosp. Electron. Syst.*, vol. 47, no. 2, pp. 1186–1202, Apr. 2011.
[24] X. Chen, J. Guan, N. Liu, and Y. He, "Maneuvering target detection via radon-fractional Fourier transform-based long-time coherent integration," *IEEE Trans. Signal Process.*, vol. 62, no. 4, pp. 939–953, Feb. 2014.
[25] R. O. Schmidt, "Multiple emitter location and signal parameter estimation," *IEEE Trans. Antennas Propag.*, vol. AP-34, no. 3, pp. 276–280, Mar. 1986.
[26] R. Roy, A. Paulraj, and T. Kailath, "ESPRIT—A subspace rotation approach to estimation of parameters of cisoids in noise," *IEEE Trans. Acoust., Speech, Signal Process.*, vol. ASSP-34, no. 5, pp. 1340–1342, Oct. 1986.
[27] R. M. Liang and K. S. Arun, "Parameter estimation for superimposed chirp signals," in *Proc. IEEE Int. Conf. Acoust., Speech, Signal Process.*, San Francisco, CA, USA, Mar. 1992, pp. 273–276.
[28] R. Tibshirani, "Regression shrinkage and selection via the lasso," *J. Roy. Statist. Soc., B Methodol.*, vol. 58, no. 1, pp. 267–288, 1996.
[29] B.-Y. Liu, "HF over-the-horizon radar system performance analysis," M.S. thesis, Dept. Inf. Sci., Nav. Postgraduate School, Monterey, CA, USA, 2007. [Online]. Available: https://apps.dtic.mil/sti/pdfs/ADA474069.pdf
[30] Y. D. Zhang, M. G. Amin, and B. Himed, "Reduced interference time-frequency representations and sparse reconstruction of undersampled data," in *Proc. Eur. Signal Process. Conf.*, Marrakech, Morocco, Sep. 2013, pp. 1–5.
[31] Y. T. H. Nguyen, D. McLernon, M. Ghogho, and S. A. R. Zaidi, "Sparse reconstruction of time-frequency representation using the fractional Fourier transform," in *Proc. Int. Conf. Recent Adv. Signal Process., Telecommun. Comput. (SigTelCom)*, Da Nang, Vietnam, Jan. 2017, pp. 16–20.
[32] S. Zhang and Y. D. Zhang, "Low-rank Hankel matrix completion for robust time-frequency analysis," *IEEE Trans. Signal Process.*, vol. 68, pp. 6171–6186, 2020.
[33] H.-B. Sun, G.-S. Liu, H. Gu, and W.-M. Su, "Application of the fractional Fourier transform to moving target detection in airborne SAR," *IEEE Trans. Aerosp. Electron. Syst.*, vol. 38, no. 4, pp. 1416–1424, Oct. 2002.
[34] B. Efron, T. Hastie, I. Johnstone, and R. Tibshirani, "Least angle regression," *Ann. Statist.*, vol. 32, no. 2, pp. 407–499, 2004.
[35] H. L. Van Trees, *Optimum Array Processing: Part IV of Detection, Estimation, and Modulation Theory*. Hoboken, NJ, USA: Wiley, 2001.

YIMIN D. ZHANG (Fellow, IEEE) received the Ph.D. degree from the University of Tsukuba, Tsukuba, Japan, in 1988.

From 1998 to 2015, he was a Research Faculty with the Center for Advanced Communications, Villanova University, Villanova, PA, USA. He is currently an Associate Professor with the Department of Electrical and Computer Engineering, Temple University, Philadelphia, PA, USA. His research interests include array signal processing, compressive sensing, machine learning, convex optimization, and time-frequency analysis with applications to radar, wireless communications, and satellite navigation. He is a fellow of SPIE. He was a recipient of the 2016 IET Radar, Sonar & Navigation Premium Award, the 2017 IEEE Aerospace and Electronic Systems Society Harry Rowe Mimno Award, the 2019 IET Communications Premium Award, and the 2021 EURASIP Best Paper Award for Signal Processing. He coauthored two articles that received the 2018 and 2021 IEEE Signal Processing Society Young Author Best Paper Awards, respectively. He was a Technical Co-Chair of the 2018 IEEE Sensor Array and Multichannel Signal Processing Workshop. He is an Associate Editor of the IEEE TRANSACTIONS ON AEROSPACE AND ELECTRONIC SYSTEMS and *Signal Processing*. He was an Associate Editor of the IEEE TRANSACTIONS ON SIGNAL PROCESSING, the IEEE SIGNAL PROCESSING LETTERS, and *Journal of the Franklin Institute*.

AMMAR AHMED (Member, IEEE) received the Ph.D. degree in electrical engineering from Temple University, Philadelphia, PA, USA, in 2021. He is currently working as a Radar Signal Processing Engineer at Aptiv PLC, Agoura Hills, CA, USA. His research interests include digital signal processing, optimization, and radar systems.

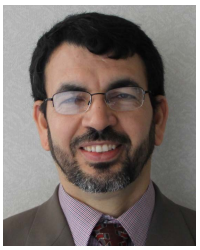

BRAHAM HIMED (Fellow, IEEE) received the Engineering degree in electrical engineering from the Ecole Nationale Polytechnique of Algiers, in 1984, and the M.S. and Ph.D. degrees in electrical engineering from Syracuse University, Syracuse, NY, USA, in 1987 and 1990, respectively. He is currently a Division Research Fellow with the Air Force Research Laboratory, Sensors Directorate, Distributed RF Sensing Branch, Dayton, OH, USA, where he is involved with several aspects of radar developments. His research interests include detection, estimation, multichannel adaptive signal processing, time series analyses, array processing, adaptive processing, waveform diversity, MIMO radar, passive radar, and over the horizon radar. He is also a fellow of AFRL (Class of 2013). He is a member of the AESS Board of Governors (2021–2023). He was a recipient of the 2001 IEEE Region I Award for his work on bistatic radar systems, algorithm development, and phenomenology. He was also a recipient of the 2012 IEEE Warren White Award for Excellence in Radar Engineering. He is also a past Chair of the AESS Radar Systems Panel.